Article

Self-Assembly of Catalytically-Active Supramolecular Coordination Compounds within Metal-Organic Frameworks

Rosa Adam, Marta Mon, Rossella Greco, Lucas H. G. Kalinke, J. Alejandro Vidal-Moya, Antonio Fernandez, Richard E. P. Winpenny, Antonio Doménech-Carbó, Antonio Leyva-Perez, Donatella Armentano, Emilio Pardo, and Jesus Ferrando-Soria

J. Am. Chem. Soc., **Just Accepted Manuscript** • DOI: 10.1021/jacs.9b03914 • Publication Date (Web): 13 Jun 2019

Self-Assembly of Catalytically-Active Supramolecular Coordination Compounds within Metal-Organic Frameworks

Rosa Adam,[§,◊] Marta Mon,[†,◊] Rossella Greco,[§] Lucas H. G. Kalinke,[†] Alejandro Vidal-Moya,[§] Antonio Fernandez,*[,‡] Richard E. P. Winpenny,[♠] Antonio Doménech-Carbó,[♦] Antonio Leyva-Pérez,*[,§] Donatella Armentano,*[,♣] Emilio Pardo*[,†] and Jesús Ferrando-Soria*[,†]

[§]Instituto de Tecnología Química (UPV-CSIC), Universidad Politècnica de València-Consejo Superior de Investigaciones Científicas, Avda. de los Naranjos s/n, 46022 Valencia, Spain.

[†]Departamento de Química Inorgánica, Instituto de Ciencia Molecular (ICMol), Catedrático José Beltrán Martínez, 2, Universidad de Valencia, 46980 Paterna, Valencia, Spain.

[‡]Chemistry Department, Sir David Davies Building, Loughborough University, Loughborough LE11 3TU, United Kingdom.

[♠]School of Chemistry and Photon Science Institute, The University of Manchester, Oxford Road, Manchester M13 9PL, United Kingdom.

[♦]Departament de Química Analítica, Universitat de València, Dr. Moliner, 50, 46100 Burjassot, València, Spain.

[♣]Dipartimento di Chimica e Tecnologie Chimiche (CTC), Università della Calabria, via P. Bucci, 12, Rende 87036, Cosenza, Italy.

◊These authors equally contributed to the work.

ABSTRACT: Supramolecular Coordination Compounds (SCCs) represent the power of Coordination Chemistry methodologies to self-assemble discrete architectures with targeted properties. SCCs are generally synthesised in solution, with isolated fully-coordinated metal atoms as structural nodes, thus severely limited as metal-based catalysts. Metal-Organic Frameworks (MOFs) show unique features to act as chemical nanoreactors for the *in-situ* synthesis and stabilization of otherwise not accessible functional species. Here, we present the self-assembly of Pd^{II} SCCs within the confined space of a preformed MOF (SCCs@MOF) and its post-assembly metalation to give a Pd^{II}-Au^{III} supramolecular assembly, crystallography underpinned. These SCCs@MOF catalyse the coupling of boronic acids and/or alkynes, representative multisite metallic-catalysed reactions in which traditional SCCs tend to decompose, and retain its structural integrity as consequence of the synergetic hybridization between SCCs and MOF. These results open new avenues in both the synthesis of novel SCCs and their use on heterogeneous metal-based Supramolecular Catalysis.

INTRODUCTION

Supramolecular chemistry methodologies have demonstrated its ability to self-assemble supramolecular coordination compounds (SCCs) with targeted properties.[1–8] An elegant exponent is catalysis within the unique confined environment of SCCs. Initially, it was inspired by nature with enzyme-mimicking approaches, and then, it expanded its interest into abiotic catalytic process merging environment catalysis with traditional homogeneous organotransition metal catalyst.[9–13] However, despite the remarkable results obtained, we consider that Supramolecular Catalysis has not yet developed with all its potential strength. This is, to some extent, directly related to the fact that the self-assembly of SCCs is done in homogenous chemistry in solution. This synthetic approach inherently induces the formation of SCCs with isolated fully-coordinated metal atoms as structural nodes, which hampers any activation of external reagents on the metal sites without destroying the assembly, thus severely limiting their use in metal-based Supramolecular Catalysis. This is exemplified by the few reactions reported with the archetypal roughly spherical polyhedra of general formula Pd_nL_{2n}, in catalytic amounts,[14–17] as well as by the need to build up ensembles with already known catalytically-active metalloligands as linkers.[18–20] Thus, a new avenue of research may be opened by finding ways to exploit the metal-catalysis of the pivotal metal atoms building the SCCs. The implementation of such a challenging task is two-fold relevant: (*i*) unprecedented functional SCCs could be developed, otherwise not accessible, which may represent a deep impact on other related research areas; and (*ii*) the catalytic potential of pivotal metal atoms could be fully unleashed, which would widen the scope of Supramolecular Catalysis.[21–23]

Metal-organic frameworks (MOFs)[24–29] have been proved as excellent platforms for a wide range of applications. This is mainly a direct consequence of two unique features of MOFs: (*i*) a rich host-guest chemistry, which can be tailored by a fine control over the size, shape and functionality of

MOFs channels,[30–35] and (*ii*) the possibility to use single-crystal X-ray crystallography as a definitive characterization tool, which offers the unique possibility – among porous materials– to contrast the success of synthetic methodologies, and even more important, to follow/understand what is actually happening within MOFs channels .[36–40] So far, this has been reflected on the considerable advances performed in such diverse fields as the adsorption and separation of guest gases[41–45] or small molecules,[46–48] and catalysis.[49–54] However, even if some advances have been recently done related with molecular recognition[55,56] and/or encapsulation of complex molecular systems,[57–59] there is still much work to be done in relation to the use of MOFs as chemical nanoreactors.[60–63] At this respect, only very few examples have been reported aiming at the MOF-driven formation of supramolecular complexes within MOFs channels, which, in addition, lack of a proper structural characterization and just models could be delivered.[64,65]

Here, we report the *in-situ* heterogeneous self-assembly, and structural characterization by single crystal X-ray diffraction (SCXRD), of three original mechanically-bonded SCCs within the unique confined space of MOF channels (SCCs@MOF). In particular, we report a novel Pd_8 square metal-organic polygon, a discrete Pd_{16} supramolecular cage and a heterobimetallic Au^{III}–Pd^{II} cage. All these robust SCCs catalyse, heterogeneously, the homocoupling of boronic acids, alkynes, and the cross-coupling between them, with higher catalytic activity and selectivity than homogeneous Pd catalysts while retaining its structural integrity, in contrast to traditional coordination cages assembled in solution. This behaviour emerges from the synergetic hybridization between SCCs and MOFs, which enables both the formation of otherwise not accessible supramolecular assemblies and its stabilization under catalytic conditions by mechanical-bonds to exploit the metal-based catalysis of pivotal metal atoms.

RESULTS AND DISCUSSION

Herein, we propose a unique template-directed strategy, involving the use of Post-Synthetic Methodologies (PSMs),[66–69] for the sequential synthesis of SCCs@MOF. Firstly, we selected as chemical nanoreactor a highly crystalline MOF, of formula $[Pd^{II}(NH_3)_4][Pd^{II}_2(\mu\text{-}O)(NH_3)_6(NH_4)_2]_{0.5}\{Ni^{II}_4[Cu^{II}_2(Me_3mpba)_2]_3\} \cdot 52H_2O$ (**1**),[61] featuring large octagonal pores (virtual diameter of *ca.* 2.0 nm) which are occupied by Pd^{II}_2 dimers, stabilized and defined, with atomic precision, to reside on preferential positions of the channels (Figure 1 left and Figure 3a center). Then, after a careful analysis –*i.e.* the available void space, the distance between Pd_2 units and the amount of available Pd^{II} ions– crystals of **1** were soaked with a solution of linear (L_1) and bended ($L_{2,3}$) ligands (Figure 1) to yield unprecedented MOF-templated *in-situ* heterogeneous self-assembled SCCs within channels. This was directly related to both, the unique confined environment provided by MOF channels, and also the presence of such uncommon dinuclear oxo-bridged palladium(II) entities in the MOFs pores.

In particular, a novel Pd^{II}_8 square metal-organic polygon of formula $[Pd^{II}_2(\mu\text{–}OH_2)_2(NH_3)_4)]_{0.5}[Pd^{II}_8(\mu\text{–}O H_2)_8(NH_3)_8(L_1)_4]_{0.125}\{Ni^{II}_4[Cu^{II}_2(Me_3mpba)_2]_3\} \cdot 43H_2O$ (**2**) was grown when using the linear ligand L_1 (Figures 2, 3a left and 3b), and with the tripodal bended ligand L_2 (Figures 3a right and 3c) a water-assisted Pd^{II}_{16} supramolecular assembly of formula $[Pd^{II}_{16}(H_2O)_8(NH_3)_{24}(\mu\text{–}OH_2)_4(H_2O)_{24}(L_2)]_{0.125}\{Ni^{II}_4[Cu^{II}_2(Me_3mpba)_2]_3\} \cdot 30H_2O$ (**3**) was obtained. Notice that L_3 has a thioether-functional group, which can act as a secondary point of coordination, once a SCC@MOF has been assembled. With L_3, the consecutive self-assembly of the supramolecular complex within MOF channels and the post-assembly metalation of the preformed SCC@MOF (Figure 1b) lead to the formation of a heterobimetallic assembly of formula $[Au^{III}_2(\mu\text{–}OH)_2(OH)_4)]_{0.5}[Au^{III}_2Cl_6Pd^{II}_2(NH_3)_6(L_3)_2]_{0.5}[Pd^{II}_2(\mu\text{-}OH_2)(NH_3)_6)]_{0.5}\{Ni^{II}_4[Cu^{II}_2(Me_3mpba)_2]_3\} \cdot 37H_2O$ (**4**) (Figures S8–S10).

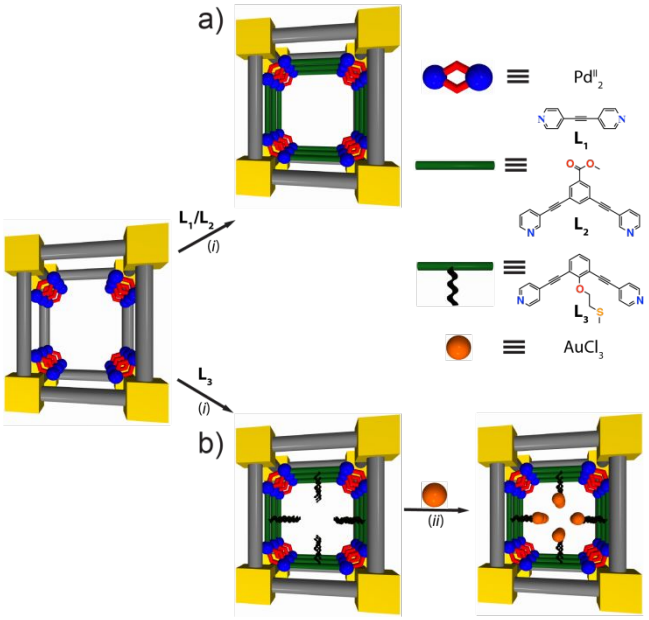

Figure 1. Template-directed strategy, involving the use of post-synthetic methodologies for the step-wise sequential synthesis of original homo- (a) and heterobimetallic (b) mechanically-bonded catalytically-active SCCs within the confined space of MOFs channels (SCCs@MOFs). (*i*) Incorporation of desired organic ligand with suitable encoded structural and coordination information and (*ii*) post-assembly metalation of preformed SCCs@MOFs.

The nature of **2**–**4** was established by the combination of a variety of different characterization techniques: inductively coupled plasma-mass spectrometry, elemental, thermo-gravimetric and powder X-Ray diffraction (PXRD) analyses, scanning electron microscopy (SEM), N_2 adsorption isotherm, Fourier transform infrared (FTIR), diffuse-reflectance (DR) UV-Vis and X-Ray photoelectron (XPS) spectroscopies (Figures S11–S17 and Table S1). Finally, the real crystal structures of **2** has been obtained by SCXRD. Even for **3** it was possible to refine a structural model which gives the most probably organization of entities self-assembled within pores. For **4**, the quality of the SCXRD data was not good enough for the complete structural resolution, but the crystallographic positions of the metal ions, building up the SCCs, and some ligand's fragments determined from Fourier maps, suggest precious

insights about the most probable structure of the growth assemblies in the confined space of **1**. This unprecedented result could be achieved thanks to both robustness and crystallinity of materials and application of cutting-edge X-ray crystallography techniques, providing, for the first time, a direct visualization of the *in-situ* heterogeneous self-assembled SCCs within MOF channels (Figures 2–4, Figures S1–S10 and Table S2).

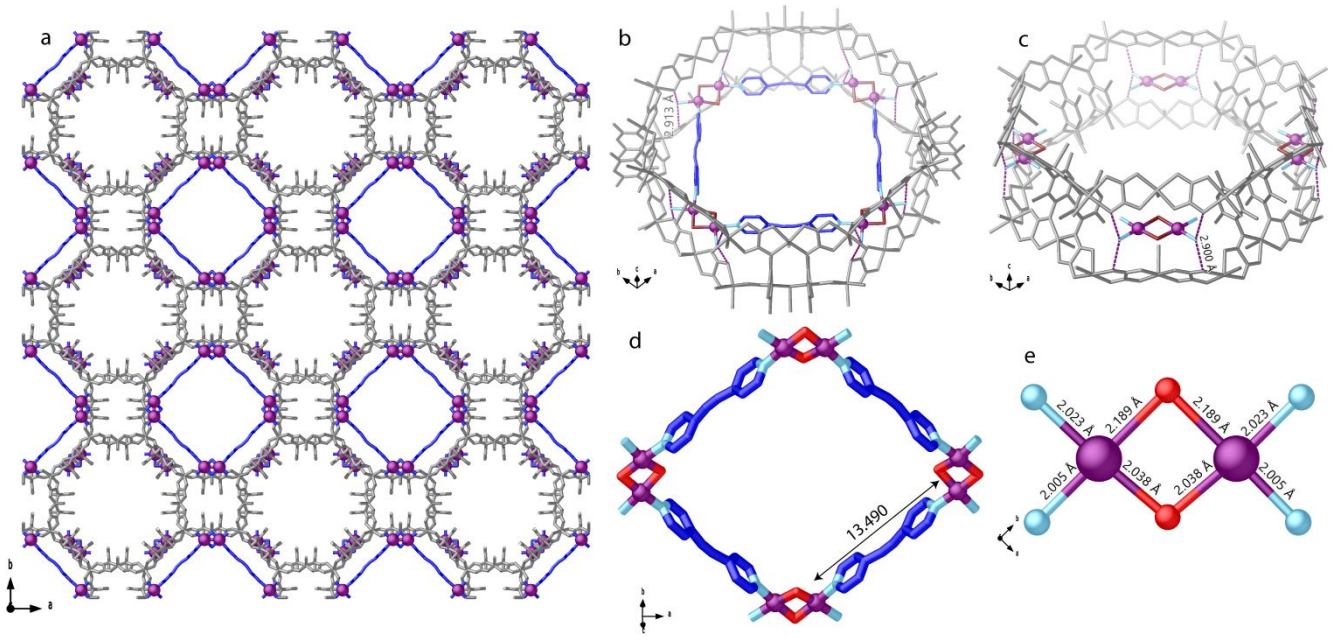

Figure 2. (a-e) Crystal structure, determined by synchrotron X-ray diffraction, of the Pd_8@MOF **2**: (a) View along *c* crystallographic axis of crystal structure of **2** (a) featuring channels filled by $[Pd^{II}_2(\mu\text{–}OH_2)_2(NH_3)_4)]^{4+}$ and $[Pd^{II}_8(\mu\text{–}OH_2)_8(NH_3)_8(L_1)_4]^{16+}$ SCCs [L_1 = 1,2-di(pyridn-4-yl)ethyne]. (b-c) Views of one single channel: Perspective views of a portion of single pores along the [111] direction showing the $[Pd^{II}_8(\mu\text{–}OH_2)_8(NH_3)_8(L_1)_4]^{16+}$ SCCs (b) and $[Pd^{II}_2(\mu\text{–}OH_2)(NH_3)_4]^{4+}$ dimers (c) and related structural parameters, stabilized by symmetric NH_3 ···O interactions. The heterobimetallic CuNi 3D anionic network is depicted as grey sticks. Pd(II) cations in the pores and ligands forming the squares and cages, are represented by purple spheres and blue sticks, respectively. Hydrogen-bonds are represented as purple dashed lines. (d-e) Details of $[Pd^{II}_8(\mu\text{–}OH_2)_8(NH_3)_8(L_1)_4]$ and $[Pd^{II}_2(\mu\text{–}OH_2)_2(NH_3)_4)]$ structures built within pores. Palladium, oxygen, carbon and nitrogen atoms are represented as violet, red, blue and pastel cyan colors.

Crystal structure. The SCXRD data of **2**–**4** evidences that the 3D network remained crystalline during the MOF-templated *in-situ* heterogeneous self-assembled process. The anionic $Ni^{II}_4Cu^{II}_6$ open-framework structure in **2**–**4** retains the known pillared square/octagonal layer architecture of **1** (Figure 2, 3 and Figures S1–S10). Both, the biggest hydrophobic octagonal channels and the square smallest pores, accommodate Pd(II) (**2**–**3**) and Pd(II)/Au(III) (**4**) complexes as result of L_1–L_3 binding to either mononuclear, $[Pd^{II}(NH_3)_4]^{2+}$, or dinuclear complexes, $[Pd^{II}_2(\mu\text{–}O)(NH_3)_6]^{2+}$, of **1** (Figures 2, 3 and Figures S1–S10). The confined assemblies in **2**–**4**, stabilized by mechanical-bonds with the MOF network, are strictly related to nature of the ligands (L) employed in terms of size, shape and imposed symmetry (see crystallographic section in Supplementary Information for structure refinement details and in-depth analysis of X-ray data).

In **2**, half of the Pd^{2+} ions from the mononuclear and dinuclear entities in **1** are self-assembled by L_1 giving $[Pd^{II}_8(\mu\text{–}OH_2)_8(NH_3)_8(L_1)_4]^{16+}$ square polygons, with $[Pd^{II}_2(\mu\text{-}OH_2)_2(NH_3)_4]$ dimers residing at the corners of the quadrangular SCC (Figures 2, 3a left, 3b and Figures S1–S5) and stabilized by H-bonds to the MOF. Each Pd(II) exhibits regular square planar geometry, with Pd–N [2.02(2) and 2.09(2) Å for Pd-N_{L1} and Pd-NH_3, respectively] and Pd-OH_2 [1.99(2) and 2.05(2) Å] bond distances similar to those found in the literature.[14–16,70] The Pd(II) separations through H_2O and L_1 bridges are 2.840(6) and 13.49(1) Å, respectively. Square polygons are regularly pillared along *c* crystallographic axes, with a Pd(II)···Pd(II) separation among adjacent polygons of 15.15(1) Å, being stabilized by mechanical-bonds with the walls of the net involving terminal NH_3 molecules and oxamate residues belonging to the net [$H_3N\cdots O_{oxamate}$ of 2.913(9) Å] (Figures S3 and S4). The synergic stabilizations ensured by hosting matrix strongly support the robustness of such assembled SCCs, with high activity in heterogeneous metal-based supramolecular catalysis (*vide infra*).

The different nature and symmetry of ligand L_2 imposes a totally different assembly in **3**, yielding a $[Pd^{II}_{16}(H_2O)_8(NH_3)_{24}(\mu\text{–}OH_2)_4(H_2O)_{24}(L_2)]$ supramolecular assembly, where $[Pd^{II}_2(NH_3)_6(L_2)]$ dimers are linked by strong hydrogen bonds, through the carboxylate group of L_2 and H_2O molecules, to $[Pd^{II}_2(\mu\text{–}OH_2)_4(H_2O)_6]$ dimers for which not all waters have been found from density maps (see Supplementary Information) [O···O of 2.89(4) and 2.89(3) Å for -COO···O_{water} and O_{water}···O_{water}, respectively] (Figures 3a right, 3c and Figures S6 and S7). Despite thermal and positional disorder detected for L_2 ligand –that clearly does not fit the space group of hosting matrix (see

Figure S7 and refinement details)– the crystal structure of SCC was solved, where Pd(II) ions exist in distorted square planar geometries with Pd-N in the $[Pd^{II}_2(NH_3)_6(L_2)]$ dimers and Pd-OH_2 distances of the $[Pd^{II}_2(\mu\text{–}OH_2)_4(H_2O)_6]$ moieties falling in the expected values [1.99(1) and 2.00(1) Å for Pd-N_{L2} and Pd-NH_3, respectively, and Pd-OH_2 of 2.05(3) and 2.47(3) Å].[14–16,70] The Pd(II)···Pd(II) separation within $[Pd^{II}_2(NH_3)_6(L_2)]$ dimers is of 6.1 Å whereas 8.3 Å is the shortest Pd(II)···Pd(II) distance detected in Pd_{16} assemblies. The strength of H-bonds observed in Pd_{16} assembly of **3**, together with its stabilization by mechanical-bonds with the network, underpins the role of supramolecular interactions in *nano*solvated space, which should be most likely able to preserve Pd_{16} aggregates during catalysis as well.

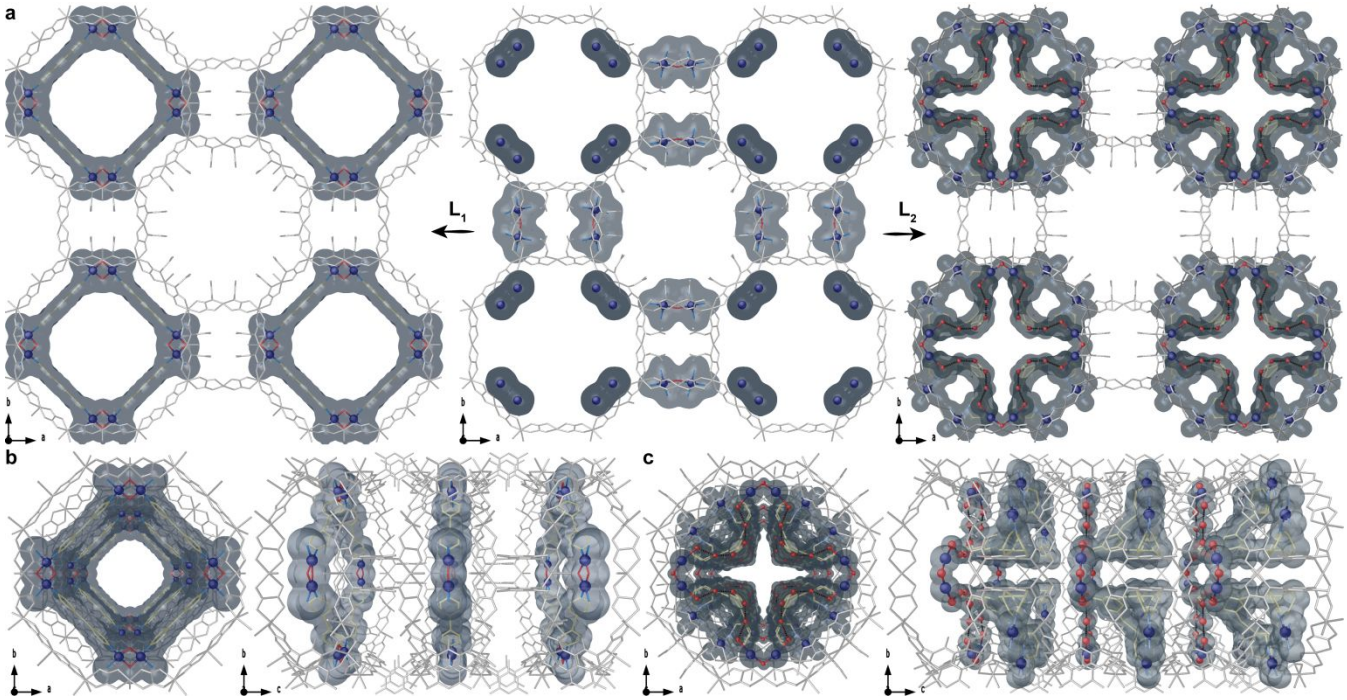

Figure 3. (a-c) Views of the crystal structures, determined by synchrotron X-ray diffraction, of the Pd_8@MOF **2** (left) and the Pd_{16}@MOF **3** (right) prepared from the *in-situ* reaction of the dipalladium(II)-containing MOF **1** (center) with the aromatic dipyridine ligands L_1 and L_2, respectively [L_1 = 1,2-di(pyridn-4-yl)ethyne and L_2 = methyl 3,5-bis(pyridine-4-ylethynyl)benzoate]. Views of one single channel of **2** (b) and **3** (c) in the *ab* (left) and *bc* (right) crystallographic planes. The heterobimetallic CuNi 3D anionic network is depicted as grey sticks. Pd(II) cations in the pores of **1**–**3** and ligands forming the squares and cages in **2** and **3**, are represented by blue spheres and gold sticks, respectively. Hydrogen-bonds that form the water-assisted Pd^{II}_{16} supramolecular assembly in **3** are represented as black dotted lines. Surfaces are used to highlight the SCCs within MOFs channels.

The quality of the SCXRD data did not allow the same precision for the complete visualization of SCCs' crystal structure of **4**. However, many local maxima attributable to Pd^{2+} and Au^{3+} metal ions in the channels together with few peaks related to L_3 ligand's fragments were located in the observed structure factor Fourier maps, providing evidence of the localization of the SCCs (Figures S8–S10 and refinement details in Supplementary Information). Looking at their disposition, it is rationale to hypothesize a self-assembly, in a similar manner as observed in **2**, producing $[Pd^{II}_2(NH_3)_6(L_3)_2]$ dimers (for which no peaks related to the aromatic moiety has been found from electron density maps) remaining in big hydrophobic pores with Pd(II) in square planar geometry [average Pd-N of 2.10(2) Å]. The Pd···Pd and N_{L3}···N_{L3} separations within dimers of 11.36 and 13.97(1) Å fit very-well with those found for complexes constructed with similar ligands (*ca.* 14 Å).[14–16] These dimers further grasp $AuCl_3$ complexes exploiting the high affinity for soft metal ions of the thioether moiety[71] featured by L_3, generating, finally, self-assembled heterometallic SCCs of the type $[Au^{III}_2Cl_6Pd^{II}_2(NH_3)_6(L_3)_2]$ showing Pd···Au and Au···Au separations of 13.50(1) and 11.89(1) Å, respectively (Figure S9). Interestingly the found position of Au(III) ions, consistent with L_3 symmetry, is displaced towards the centre of the big pores, suggesting a high accessibility for reactants. Furthermore, the solved crystal structure clearly evidences thioether fragments, allowing to unveil the Au-S distance of 2.34(1) Å.

PXRD, TGA experiments and N_2 adsorption isotherms. The experimental PXRD patterns of **2**–**4** are identical to the corresponding calculated ones (Figures S11–S12). This fact confirms the homogeneity of the bulk samples, which are isostructural to the crystals selected for single crystal X-ray diffraction. The solvent contents of **2**–**4** were established by thermogravimetric analysis (TGA) under dry N_2 atmosphere and compared to that of the ancestor compound **1** (Figure S13). Overall, it shows a fast mass loss for **1**–**4** from room temperature followed by a *pseudo* plateau until decomposition starts. Noteworthy, it is observed a greater thermal stability of **2**–**4** respect **1**, which further reinforce the beneficial synergetic hybridization in

SCCs@MOFs. The observed weight losses of 25.72 (**1**), 21.73 (**2**), 16.47 (**3**) and 15.73% (**4**), respectively, correspond to 52, 43, 30 and 37 water molecules, respectively, in line with that determined by CHN(S) analyses (see Supplementary Information). Figure S14 shows the N_2 adsorption isotherms of **1**–**4** at 77 K. They are consistent with the decrease in accessible void space in **2** and, more significantly, in **3** and **4**, suggested by the TGA analyses and the crystal structures, which is a direct consequence of the formation of largest supramolecular assemblies.

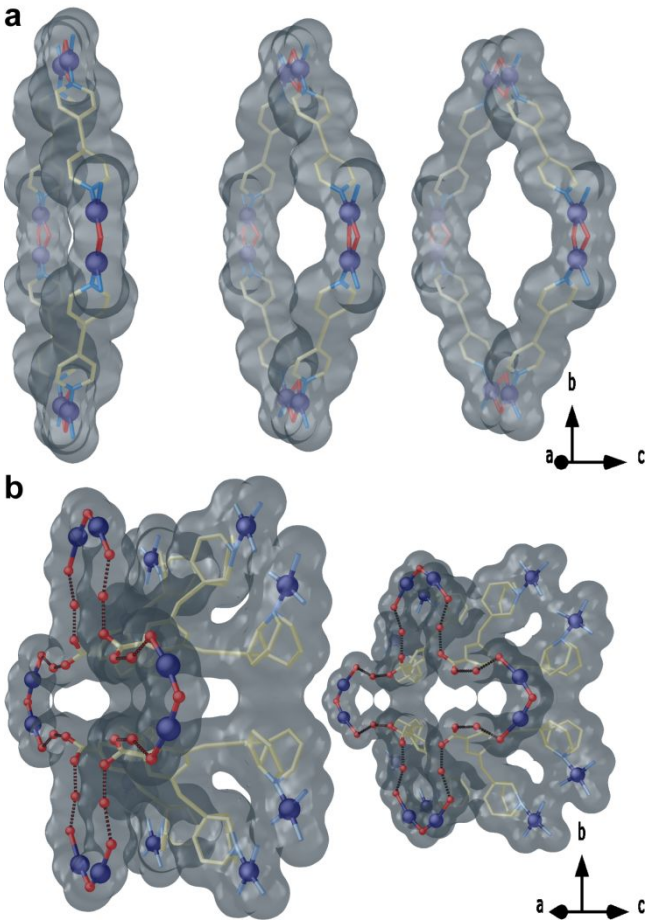

Figure 4. Supramolecular coordination compounds crystal structure. Perspective views of three Pd^{II}_8 squares (a) and two Pd^{II}_{16} (b) supramolecular cages, unveiled by single crystal X-ray diffraction, formed within one single channel of the frameworks of **2** and **3**, respectively.

MAS solid ^{13}C NMR, DR-UV-vis, FT-IR, Raman and XPS. Figure S15 shows the magic angle spinning solid ^{13}C nuclear magnetic resonance (MAS solid ^{13}C NMR) of MOF **1** and SCCs@MOFs **2**–**4**. It can be clearly seen the appearance of new and sharper signals at 165, 150 and 90 ppm in **2**, which nicely fit the expected values for the L_1 ligand, together with the signals at -40, 40, 130 and 230 ppm corresponding to the framework amides, shifted and broaden by the paramagnetic action of the Cu^{II} metal ions. Similar spectra were recorded for SCC@MOF **3** and **4**. Additionally, **4** spectrum shows a signal at 70 ppm fitting with the typical chemical shift expected for ether functionalities. Diffuse-reflectance UV-visible measurements of **2**–**4** show the loss of the palladium(II) adsorption band at λ_{max} = 320 nm observed in **1** and the appearance of three new bands at λ_{max} = 270, 300 and 350 nm (Figure S16), which agree with both the formation of SCCs and the observed bands of a previously reported $Pd^{II}_4(L_1)_4$ square SCC in solution (see Figure S20).[72] Fourier-transformed infrared spectroscopy (FT-IR) further confirms the integrity of the structural organic parts of the SCCs@MOFs in **2**–**4** together with the appearance of new signals assignable to L_{1-3} (Figure S17). Raman spectroscopy confirms the formation of the new Au-S bond by the appearance of typical bands for Au-S bonds between 200-300 and 550 cm^{-1} (Figure S18) when exciting with a 514 nm laser light.[73] X-ray photoelectron spectroscopy (XPS) shows that the $Pd3d_{5/2}$ peak of the Pd^{II} atoms (338.6 eV) in **1** slightly shifts for **2**–**4** (338.3, 338.5 and 338.1 eV, respectively), as expected by the action of the L_{1-3} ligands (Figure S19).[74] These results perfectly agree with SCXRD and give us tools to follow catalysed reactions within the solids.

Catalytic performance of SCCs@MOFs. Oligo- and poly-thiophenes are well-known conducting molecules with applications in, for instance, solar cells.[75] Their synthesis relies on the Pd-catalysed homocoupling of thienylboronic acids, a challenging C-C bond-forming reaction that requires strong bases and oxidants in the presence of a poisoning sulphur group.[76] Figure 5 shows the results for the homocoupling of two different thienylboronic acids –**5a** and **5b**– with a representative Pd(II) complex catalyst,[77] the soluble SCC $Pd^{II}_4(L_1)_4$,[72] **1**–**3** (Tables S3–S4 and Figures S20–21). SCCs@MOFs catalysts show much better activity and selectivity to **6a** than the homogeneous Pd catalysts and MOF **1**, with good recyclability and, in addition, are able to catalyse the homocoupling of other boronic acids (Figure S22). PXRD, DR UV-vis and MAS solid ^{13}C NMR measurements of **2** and **3** after reaction show identical spectra to the fresh samples, plus the signals corresponding to the polymeric product **6b** when starting from **5b** (Figure 5d, Figures S12 and S21). These results strongly support that the SCCs retain their structural integrity within the MOF during reaction and are true catalysts for homocoupling of boronic acids.

In order to better understand the stability of SCCs@MOFs under such challenging reaction conditions, mechanistic studies comparing them with their soluble counterpart $Pd^{II}_4(L_1)_4$ were performed. The kinetic equation rate is first order in all reagents for **2** and **3**, but half order respect to Pd and second order for benzoquinone for soluble $Pd^{II}_4(L_1)_4$ (Figure 6a, Figures S23–S27).[76,78] *In-situ* ^{1}H NMR measurements show the rapid degradation of soluble $Pd^{II}_4(L_1)_4$ after addition of **5a**, with release of free L_1 to the medium and coordination of benzoquinone to Pd^{II} ions while the reaction occurs[78] (Figure 5e, Figure S28). Any attempt to re-assemble $Pd^{II}_4(L_1)_4$ produces a linear decrease of the initial rate (Figure S29) and O_2 is required as an oxidant (Tables S5 and S6),[77,79] which is not the case in the heterogeneous coupling. These results show that $Pd^{II}_4(L_1)_4$ is just a precursor of the Pd catalytic species while, in clear contrast, **2** and **3** remain untouched and catalytically active during the heterogeneous reaction.

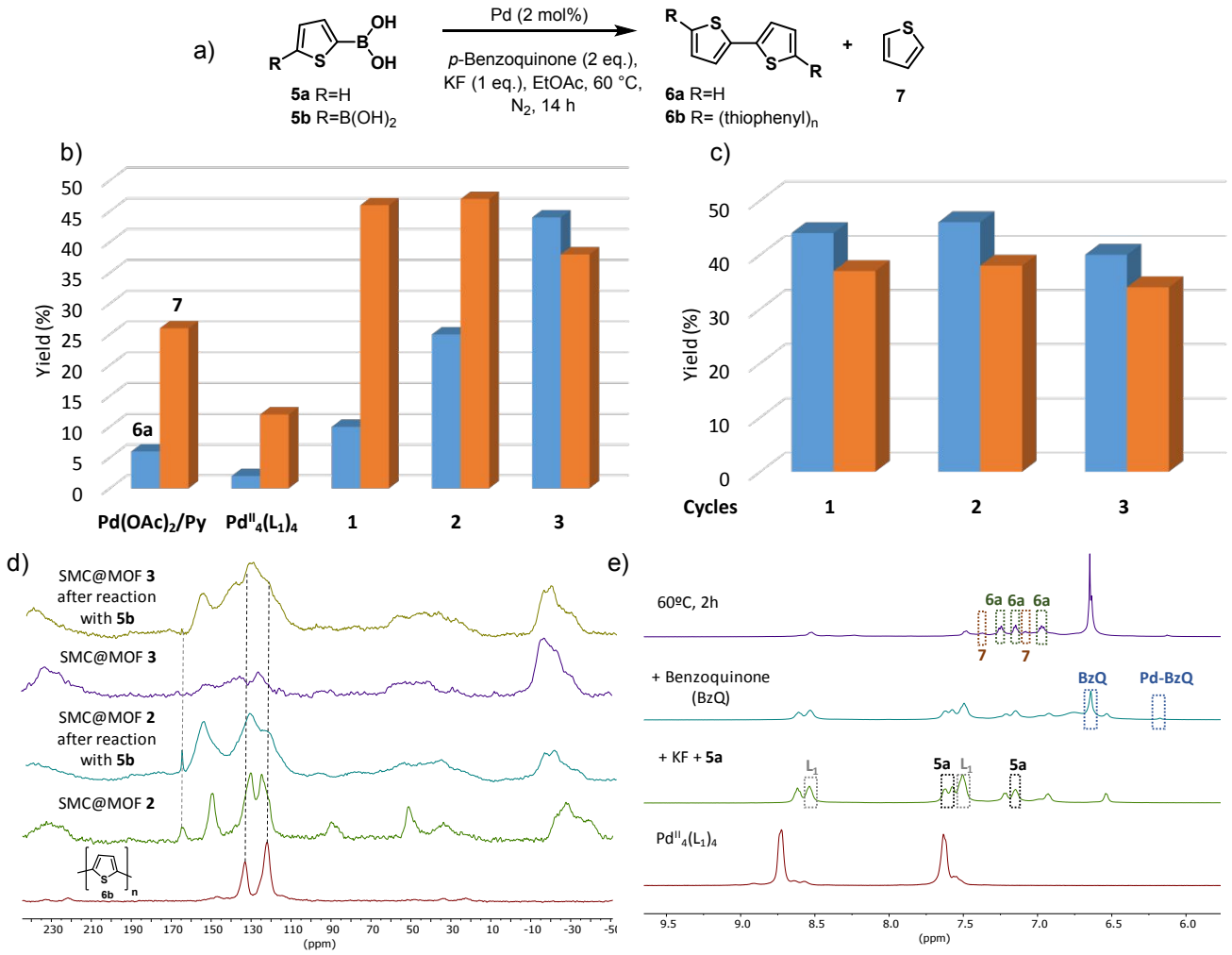

Figure 5. (a) Homocoupling of thienylboronic acids **5a** and **5b** in the presence of 2 mol % of Pd, **5a-b** (0.1 mmol), KF (0.1 mmol, 5.8 mg), *p*-benzoquinone (0.2 mmol, 21.6 mg), EtOAc (1.5 mL) and dodecane (10 μL) as internal standard, under N_2, at 60ºC, during 14h. (b) Yields of **6a** and **7** in the homocoupling of **5a** catalyzed by $Pd(OAc)_2$/Py (1/1), $Pd_4(L_1)_4$, MOF **1**, SCC@MOF **2** and **3**. (c) Reuses for SCC@MOF **3** in the homocoupling of **5a**. (d) From bottom to top: MAS solid ^{13}C NMR of polymer **6b**, SCC@MOF **2**, SCC@MOF **2** after reaction with **5b**, SCC@MOF **3** and SCC@MOF **3** after reaction with **5b**. (e) Aromatic area of $Pd_4(L_1)_4$ ^1H NMR spectra (CD_3CN/D_2O) after the sequential addition of KF (2 eq), **5a** (2 eq) and benzoquinone (2 eq) and the treatment of the mixture at 60 ºC during 2 h.

XPS measurements after treating **2** and **3** inside the chamber with an O_2 atmosphere do not show any Pd^{IV} signals (Figure 6b). Cyclic voltammetry of **3** during the reaction of **5a** shows that the cathodic signal assignable to the Pd^{II} atoms of the SCC@MOF ($C_{Pd(II)}$) evolves to a new signal corresponding to Pd^{I} ($C_{Pd(I)}$), significantly different to the signals of coupling product **6a**, redox active benzoquinone and uncatalysed product **7** (Figure 6c, for blank experiments see Figures S30 and S31). This bimetallic Pd^{I}/Pd^{II} redox manifold, without the involvement of Pd^0 or Pd^{IV} species, avoids extensive structural distortions in the mechanically-bonded assemblies and, hence, further contributes to retain their integrity during the coupling. Overall, the combined kinetic, spectroscopic and electrochemical results enable us to propose a mechanism for the homocoupling of boronic acids catalysed by **2** and **3** (Figure 6d), where the confined Pd^{II}_2 units catalyse the homocoupling reaction by a redox cooperative mechanism in which both Pd^{II} metal ions reduce to Pd^{I}, releasing **6**, and finally re-oxidize to the original form.

a)

$$r_0 = k_{app} \cdot [\mathbf{5a}]^{\alpha} \cdot [Pd\ cat.]^{\beta} \cdot [Benzoquinone]^{\gamma} \cdot [KF]^{\delta}$$

Catalyst	α	β	γ	δ
2	1	1	1	1
3	1	1	1	1
$Pd_4(L_1)_4$	1	1/2	2	1

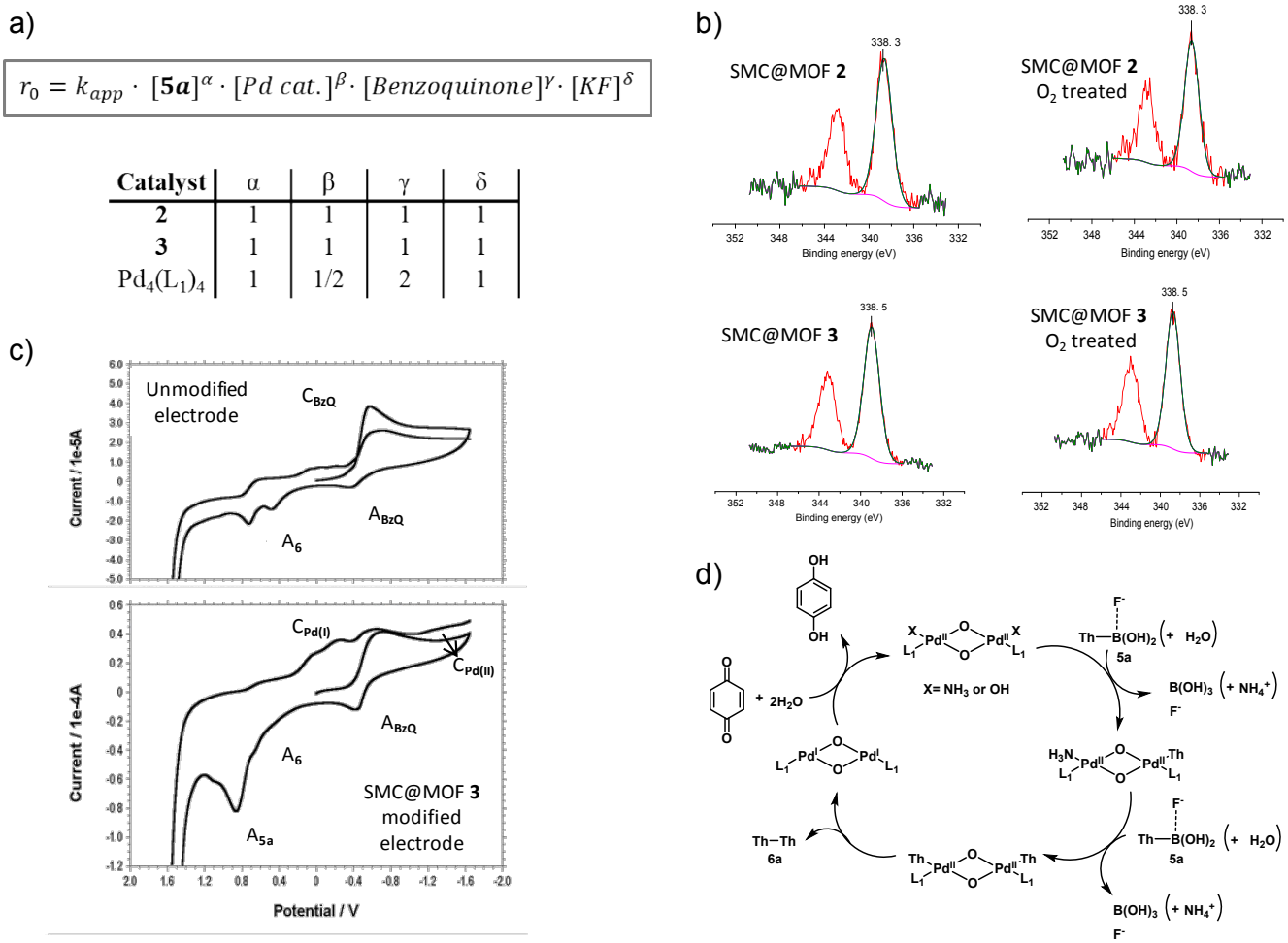

Figure 6. (a) Kinetic equation rate and kinetic parameters for the homocoupling of thienylboronic acid **5a** calculated through initial rate values for **2**, **3** and $Pd^{II}_4(L_1)_4$. Reaction conditions: **5a** (0.4–0.8 mmol), KF (0–1.6 mmol), *p*-benzoquinone (0–1.6 mmol), catalyst (0–2 mol%), dodecane (40 μL), EtOAc (6 mL) for SCC@MOF **2** and **3** or CH_3CN (6 mL) for $Pd^{II}_4(L_1)_4$, N_2, 60ºC. (b) X–ray photoelectron spectroscopy (XPS) of SCCs@MOFs **2** (top) and **3** (bottom), before (left) and after (right), treatment in the chamber with O_2 for 30 minutes. (c) *In-situ* cyclic voltammograms of a solution of **5a** (1 mM), KF (1 mM) and benzoquinone (1 mM) in 0.10 M Bu_4NPF_6/MeCN before (top) and after (bottom) modifying glassy carbon electrodes with SCC@MOF **3**, *A* stands by anodic signals and *C* stands by cathodic signals, potential scan rate was 50 mV s^{-1}. (d) Postulated mechanism for the homocoupling of thienylboronic acid **5a** catalyzed by the Pd_2 moieties in SCC@MOF **2**.

Following this mechanistic rationale, **2**, **3**, and also the heterobimetallic $Au^{III}Pd^{II}$ **4** (Figure 7a, Tables S7 and S8), were tested as catalysts for the coupling of alkynes.[80] The three SCCs@MOFs were more active for homocoupling of phenylacetylene **8a** than the homogeneous Pd catalysts tested as well as than MOF **1**, with **4** affording the better selectivity to **9a**. Moreover, **4** proved its utility through the homocoupling of a series of alkynes **8b-e** and the cross coupling of phenylacetylene **8a** with **8f-h**, affording diynes **9b-h** with moderate to good yields (Figure 7d, Figures S32 and S33). Notice that a related MOF with supported thio-alkyl Au^{III} complexes, not containing Pd atoms, does not show any catalytic activity.[71] Kinetic and ^1H NMR experiments (Figures S34–S40) confirm that, as occurs for homocoupling of **5a**: (*i*) homocoupling of **8a** is first order kinetics for **4** but ½ for $Pd^{II}_4(L_1)_4$ (Figure 7b), (*ii*) $Pd^{II}_4(L_1)_4$ readily decomposes after the addition of the reagents (Figure 7c, Figure S40), and (*iii*) O_2 has more influence for the decomposed $Pd^{II}_4(L_1)_4$ than for **4** (Figures S35 and S38).[81] Kinetic isotope effect (KIE) for **8a** is 3.4(7) and 0.9(1) for catalysts **4** and $Pd^{II}_4(L_1)_4$, respectively (Figures S36 and S39), which nicely fits the observation that **8a** only intervenes in the equation rate of catalyst **4** and not of $Pd^{II}_4(L_1)_4$.[82] Following this, **2**–**4** were tested for the more challenging cross-coupling between boronic acid **5a** and alkyne **8a** (Figure 7e),[83] showing moderate conversions and selectivity, in any case higher than the homogeneous catalysts and the simpler MOF **1** (Figure 7e and Figure S41). In order to showcase the practical advantages of the SCCs@MOFs respect to other soluble and/or MOF catalysts, the homocoupling of **8a** was carried out in a fixed-bed tubular reactor with **4** as a solid catalyst. The results (Figure S42) show that, indeed, alkyne **8a** transforms to the homocoupling product **9a** in flow, thus allowing to the production of diynes in continuous flow, a process difficult to achieve with other solid catalysts that make use of solid bases[84] or that, simply, are soluble and not solid.[85]

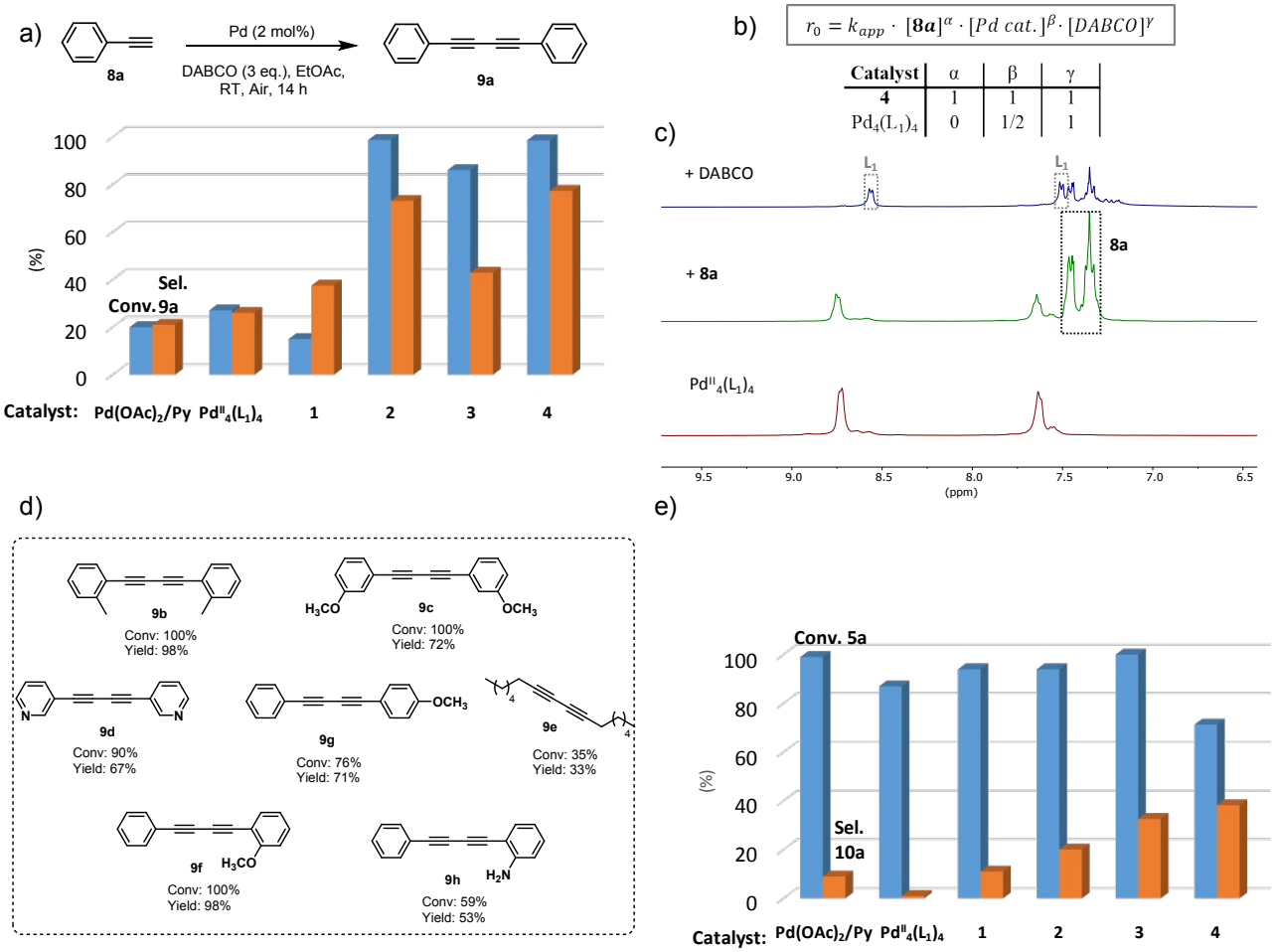

Figure 7. (a) Phenylacetylene **8a** conversion and diphenylbutadiyne **9a** yield for the homocoupling of **8a** catalyzed by $Pd(OAc)_2$/Py (1/1), $Pd_4(L_1)_4$, MOF **1** and SCC@MOF **2**-**4**. Reaction conditions: 2 mol % of Pd, **8a** (0.1 mmol, 10.1 mg), DABCO (0.3 mmol, 33.6 mg), EtOAc (1.5 mL) and dodecane (10 μL) as an internal standard, under air atmosphere, at RT, during 14 h. (b) Kinetic equation rate and kinetic parameters for the homocoupling of phenylacetylene **8a** calculated through initial rate values for **4** and $Pd^{II}_4(L_1)_4$. Reaction conditions: **8a** (0.4–0.8 mmol), DABCO (0–2.4 mmol), catalyst (0–2 mol% Pd), dodecane (40 μL), EtOAc (6 mL) for SCC@MOF **4** or CH_3CN (6 mL) for $Pd^{II}_4(L_1)_4$, air, 60 ºC; (c) Aromatic area of $Pd_4(L_1)_4$ ^{1}H NMR spectra (CD_3CN/D_2O) after the sequential addition (from bottom to top) of **8a** (2 eq) and DABCO (2 eq); (d) Substrate scope for the homocoupling of alkynes **8b**-**e** and the cross coupling between phenylacetylene **8a** and alkynes **8f**-**h** catalyzed by SCC@MOF **4** (reaction conditions shown in the Supporting Information); (e) Thienylboronic acid **5a** conversion and **10a** yield for the cross coupling between **5a** and **8a** catalyzed by $Pd(OAc)_2$/Py (1/1), $Pd_4(L_1)_4$, MOF **1** and SCC@MOF **2**-**4**. Reaction conditions: 2 mol% of Pd, **5a** (0.1 mmol, 12.8mg), **8a** (0.3 mmol, 30.3 mg), KF (0.1 mmol, 5.8 mg), *p*-benzoquinone (0.2 mmol, 21.6 mg), DABCO (0.9 mmol, 100.9 mg), EtOAc (1.5 mL) and dodecane (10 μL) as internal standard, under air atmosphere, at 60 ºC, during 14 h.

CONCLUSIONS

We report a unique synthetic strategy for the template-directed sequential construction of novel stable supramolecular complexes within a MOF channels, SCCs@MOF, taking advantage of the singular confined environment provided by MOF channels, and also the presence of such uncommon dinuclear Pd(II) entities in the MOFs pores. As proof-of-concept, we have synthesised and crystallographically characterized three original constructs mechanically-bonded to a MOF network, never obtained before outside the MOFs. In particular, we report a novel Pd_8 square metal-organic polygon, fully characterized by SCXRD, a discrete Pd_{16} supramolecular cage and a heterobimetallic Au^{III}–Pd^{II} cage, underpinned by SCXRD. These solid SCCs catalyse the coupling of boronic acids and alkynes, while keeping the SCCs structure untouched, with better catalytic activity and selectivity than standard Pd catalysts and soluble $Pd^{II}_4(L_1)_4$ squares, the latter readily decomposing under reaction conditions. Overall, this work, represents a general versatile approach, easily extendable to other metals and ligands, for the assembly of original supramolecular constructs with great potential in heterogeneous metal-based Supramolecular Catalysis.

EXPERIMENTAL SECTION

Materials. 1,2-di(pyridin-4-yl)ethyne (L_1), methyl 3,5-bis(pyridin-4-ylethynyl)benzoate (L_2), $\{[Pd^{II}(en)(L_1)]_4(NO_3)_8\}$ ($Pd^{II}_4(L_1)_4$)[72] and $[Pd^{II}(NH_3)_4][Pd^{II}_2(\mu$–$H_2O)(NH_3)_6]_{0.5}\{Ni^{II}_4[Cu^{II}_2(Me_3mpba)_2]_3\} \cdot 52H_2O$ (**1**)[61] were prepared according to literature procedure (see Suplementary Methods).

Synthesis. A detailed description for the synthesis 4,4'-((2-(2-(methylthio)ethoxy)-1,3-phenylene)bis(ethyne-2,1-diyl))dipyridine (L_3) is given in the Supplementary Methods. For $[Pd^{II}_2(\mu$–$OH_2)_2(NH_3)_4)]_{0.5}[Pd^{II}_8(\mu$–$O H_2)_8(NH_3)_8(L_1)_4]_{0.125}\{Ni^{II}_4[Cu^{II}_2(Me_3mpba)_2]_3\} \cdot 43H_2O$ (**2**). Well–formed deep green prisms of **2**, which were suitable for X–ray diffraction, were obtained by immersing crystals of **1** (*ca.* 36 mg, 0.010 mmol) in hot (50 °C) acetonitrile solutions of L_1 (5 mL, 10 mM) for one week. Then, the supernatant solution was removed, and the crystals were washed with an acetonitrile solution (5 x 10 mL), isolated by filtration on paper and air–dried. Alternatively, large scale syntheses of **2**, were also carried out by using the same synthetic procedure but with stirring and with greater amounts of both, a powder sample of compound **1** (2 g, 0.55 mmol) and L_1 (50 mL, 55 mM), with the same successful results. Finally, the product was collected by filtration, washed with a acetonitrile solution and air–dried. Elemental analysis [% calcd., % found for $Cu_6Ni_4Pd_2C_{84}H_{163}N_{16}O_{81}$ (3522.17)]: C, 28.65; H, 4.67; N, 6.36%. Found: C, 28.75; H, 4.72; N, 6.31%. IR (KBr): ν = 1603 cm^{-1} (C=O).

For $[Pd^{II}_{16}(H_2O)_8(NH_3)_{24}(\mu$–$OH_2)_4(H_2O)_{24}(L_2)]_{0.125}\{Ni^{II}_4[Cu^{II}_2(Me_3mpba)_2]_3\} \cdot 30H_2O$ (**3**). The compound **3** was prepared by an analogous procedure to that for **2** by using L_2 as precursor instead of L_1. Elemental analysis [% calcd., % found for $Cu_6Ni_4Pd_2C_{80.75}H_{139.75}N_{15.25}O_{70.75}$ (3285.2)]: C, 29.50; H, 4.25; N, 6.50%. Found: C, 29.39; H, 4.08; N, 6.23%. IR (KBr): ν = 1601 cm^{-1} (C=O).

For $[Au^{III}_2(\mu$–$OH)_2(OH)_4)]_{0.5}[Au^{III}_2Cl_6Pd^{II}_2(NH_3)_6(L_3)_2]_{0.5}[Pd^{II}_2(\mu$-$OH_2)(NH_3)_6)]_{0.5}\{Ni^{II}_4[Cu^{II}_2(Me_3mpba)_2]_3\} \cdot 37H_2O$ (**4**). Well–shaped deep green prisms of **4**, were obtained by immersing crystals of **1** (*ca.* 36 mg, 0.010 mmol) in hot (50 ºC) acetonitrile solutions of L_3 (5 mL, 10 mM) for one week. After washing the crystals with additional acetonitrile (5 x 10 mL), they were immersed in a fresh H_2O/CH_3OH (1:1) solution. The solution was exchanged every three hours five times. Then, the crystals were treated in a H_2O/CH_3OH (1:1) solution of $AuCl_3$ (3.0 mg, 0.010 mmol) for 12 hours. The process was repeated five more times to ensure that the maximum loading of possible gold atoms was achieved. This was monitored by ICP-MS and SEM/EDX. The gold-metallated crystals had the same size and shape as those of the starting SCC@MOF, ruling out a possible dissolution-recrystallization mechanism for this system and strongly suggesting a solid-state process in the formation of the heterobimetallic SCC@MOF. The crystals were washed with a H_2O/CH_3OH (1:1) solution (5 x 10 mL), isolated by filtration on paper and air–dried. Alternatively, large scale syntheses of **4**, were also carried out by using the same consecutive step-by-step synthetic procedure but with stirring and with greater amounts of precursors, a powder sample of compound **1** (2 g, 0.55 mmol), L_3 (50 mL, 55 mM) and $AuCl_3$ (0.17 g, 0.55 mmol) with the same successful results. The metalation of the preformed SCC@MOF was repeated five times. This was monitored by ICP-MS and SEM/EDX. Finally, the product was collected by filtration, washed with a H_2O/CH_3OH (1:1) solution and air–dried. Elemental analysis [% calcd., % found for $Cu_6Ni_4Pd_2Au_2C_{101}H_{174}N_{20}O_{77.5}$ (4269.8)]: C, 28.39; H, 4.08; S, 0.75; N, 6.56%. Found: C, 28.85; H, 4.33; S, 0.90; N, 6.80%. IR (KBr): ν = 1603 cm^{-1} (C=O).

Single crystal X-ray diffraction. Diffraction data for **2** and **4** were collected using synchrotron radiation at I19 beamline of the Diamond Light Source at λ = 0.6889 Å, whereas for **3** on a Bruker-Nonius X8APEXII CCD area detector diffractometer using graphite-monochromated Mo-K_α radiation (λ = 0.71073 Å). Crystal data for **2**–**4**: tetragonal, space group P4/*mmm*, T = 30(2) for **2** and **4** and 90(2) K for **3**, Z = 4. **2**: $C_{84}H_{163}Cu_6N_{16}Ni_4O_{81}Pd_2$, a = 35.7158(2) Å, c = 15.14950(10) Å, V = 19325.0(3) $Å^3$; **3**: $C_{80.75}H_{139.75}Cu_6N_{15.25}Ni_4O_{70.75}Pd_2$, a = 35.258(10) Å, c = 15.119(4) Å, V = 18795(12) $Å^3$; **4**: $C_{101}H_{174}Cu_6N_{20}Ni_4O_{77.5}SPd_2Au_2Cl_3$, a = 35.725(2) Å, c = 15.2666(8) Å, V = 19485(2) $Å^3$. Further details can be found in the Supplementary Information.

CCDC 1892911, 1892912 and 1892914 for **2**, **3** and **4**, respectively contain the supplementary crystallographic data for this paper. These data can be obtained free of charge *via* www.ccdc.cam.ac.uk/conts/retrieving.html (or from the Cambridge Crystallographic Data Centre, 12 Union Road, Cambridge CB21EZ, UK; fax: (+44)1223-336-033; or deposit@ccdc.cam.ac.uk).

^1H and ^{13}C NMR Spectroscopy, Magic Angle Spinning Solid ^{13}C NMR Spectroscopy, Diffuse-reflectance UV-Vis, Infrared Spectroscopy, Microscopy measurements, X–ray Powder Diffraction Measurements, X–ray photoelectron spectroscopy (XPS) measurements and Electrochemical Measurements. A detailed description of all the different characterization techniques used is given in the Supplementary Information.

Catalytic Experiments. A detailed description of all the catalytic experiments is given in the Supplementary Information.

ASSOCIATED CONTENT

Supporting Information Available. Physical techniques. Crystallographic refinement and catalytic details. Figures S1–S42. Tables S1–S8. CCDC reference numbers: CCDC–1892911, 1892912 and 1892914. This material is available free of charge via the Internet at http://pubs.acs.org.

AUTHOR INFORMATION

Corresponding Author

* To whom correspondence should be addressed. E–mail: jesus.ferrando@uv.es; anleyva@itq.upv.es; donatella.armentano@unical.it; a.fernandez-mato@lboro.ac.uk; emilio.pardo@uv.es.

Notes

The authors declare no competing financial interests.

ACKNOWLEDGMENT

This work was supported by the MINECO (Spain) (Projects CTQ2016–75671–P, 2017–86735–P and Excellence Units "Severo Ochoa" and "Maria de Maeztu" SEV–2016–0683 and MDM–2015–0538), the Ministero dell'Istruzione, dell'Università e della Ricerca (Italy) and the Engineering and Physical Sciences Research Council (UK). M.M. thanks the MINECO for a predoctoral contract. R.A. thanks UPV and R.G. thanks ITQ for the corresponding contracts. D.A. thanks the "Fondo per il finanziamento delle attività base di ricerca". E.P. acknowledges the financial support of the European Research Council under the European Union's Horizon 2020 research and innovation programme / ERC Grant Agreement No 814804, MOF-reactors. Thanks are also extended to the "Subprograma Atracció de Talent-Contractes Post-doctorals de la Universitat de Valencia" and the "2018 Leonardo Grant for Researchers and Cultural Creators, BBVA Foundation" (J.F.S.). We thank Diamond Light Source for awarded beamtime (proposal number MT18768) and provision of synchrotron radiation facility and Dr David Allan and Dr Sarah Barnett for their assistance at I19 beamline.

REFERENCES

(1) Lehn, J.-M. *Supramolecular Chemistry: Concepts and Perspectives*; Wiley-VCH, Weinheim, **1995**.

(2) Steed, J. W.; Atwood, J. L. *Supramolecular Chemistry*; John Wiley & Sons, Chichester, **2000**.

(3) Chakrabarty, R.; Mukherjee, P. S.; Stang, P. J. Supramolecular Coordination: Self-Assembly of Finite Two- and Three-Dimensional Ensembles. *Chem. Rev.* **2011**, *111*, 6810–6918.

(4) Ward, M. D.; Raithby, P. R. Functional behaviour from controlled self-assembly: challenges and prospects. *Chem. Soc. Rev.* **2013**, *42*, 1619–1636.

(5) Roberts, D. A.; Pilgrim, B. S.; Nitschke, J. R. Covalent post-assembly modification in metallosupramolecular chemistry. *Chem. Soc. Rev.* **2018**, *47*, 626–644.

(6) Howlader, P.; Mondal, B.; Purba, P. C; Zangrando, R.; Mukherjee, P. S. Self-Assembled Pd(II) Barrels as Containers for transient Merocyanine Form and Reverse Thermochromism of Spiropyran. *J. Am. Chem. Soc.* **2018**, *140*, 7952–7960.

(7) Chakraborty, S.; Newkome, G. R. Terpyridine-based metallosupramolecular constructs: tailored monomers to precise 2D-motifs and 3D-metallocages. *Chem. Soc. Rev.* **2018**, *47*, 3991–4016.

(8) Zhou, Z.; Chen, D.-G.; Saha, M. L.; Wang, H.; Li, X.; Chou, P.-T.; Stang, P. J. Designed Conformation and Fluorescence Properties of Self-Assembled Phenazine-Cored Platinum(II) Metallacycles. *J. Am. Chem. Soc.* **2019**, *141*, 5535–5543.

(9) Cullen, W.; Misuraca, M. C.; Hunter, C. A.; Williams, N. H.; Ward, M. D. Highly efficient catalysis of the Kemp elimination in the cavity of a cubic coordination cage. *Nat. Chem.* **2016**, *8*, 231–236.

(10) Howlader, P.; Das, P.; Zangrando, R.; Mukherjee, P. S. Urea-Functionalized Self-Assembled Molecular Prism for Heterogeneous Catalysis in Water. *J. Am. Chem. Soc.* **2016**, *138*, 1668–1676.

(11) Ueda, Y.; Ito, H.; Fujita, D.; Fujita, M. Permeable Self-Assembled Molecular Containers for Catalyst Isolation Enabling Two-Step Cascade Reactions. *J. Am. Chem. Soc.* **2017**, *139*, 6090–6093.

(12) Pilgrim, B. S.; Roberts, D. A.; Lohr, T. G.; Ronson, T. K.; Nitschke, J. R. Signal transduction in a covalent post-assembly modification cascade. *Nat. Chem.* **2017**, *9*, 1276–1281.

(13) Hong, C. M.; Bergman, R. G.; Raymond, K. N.; Toste, F. D. Self-Assembled Tetrahedral Hosts as Supramolecular Catalysts. *Acc. Chem. Res.* **2018**, *51*, 2447–2455.

(14) Tominaga, M.; Suzuki, K.; Kawano, M.; Kusukawa, T.; Ozeki, T.; Sakamoto, S.; Yamaguchi, K.; Fujita M. Finite, spherical coordination networks that self-organize from 36 small components. *Angew. Chem. Int. Ed.,* **2004**, *43*, 5621–5625.

(15) Sun, Q.-F.; Iwasa, J.; Ogawa, D.; Ishido, Y.; Sato, S.; Ozeki, T.; Sei, Y.; Yamaguchi, K.; Fujita, M. Self-Assembled $M_{24}L_{48}$ Polyhedra and Their Sharp Structural Switch upon Subtle Ligand Variation. *Science*, **2010**, *328*, 1144–1147.

(16) Fujita, D.; Ueda, Y.; Sato, S.; Mizuno, N.; Kumasaka, T.; Fujita, M. Self-assembly of tetravalent Goldberg polyhedra from 144 small components. *Nature* **2016**, *540*, 563–566.

(17) Pradhan, S.; John, R. P. Self-assembled Pd_6L_4 cage and Pd_4L_4 square using hydrazide-based ligands: synthesis, characterization and catalytic activity in Suzuki-Miyaura coupling reactions. *RSC Adv.* **2016**, *6*, 12453–12460.

(18) Lee, S. J.; Cho, S.-H.; Mulfort, K. L.; Tiede, D. M.; Hupp, J. T.; Nguyen, S. T. Cavity-Tailored, Self-Sorting Supramolecular Catalytic Boxes for Selective Oxidation. *J. Am. Chem. Soc.* **2008**, *130*, 16828–16829.

(19) Li, H.; Han, Y.-F.; Lin, Y.-J.; Guo, Z.-W.; Jin, G.-X. Stepwise Construction of Discrete Heterometallic Coordination Cages Based on Self-Sorting Strategy. *J. Am. Chem. Soc.* **2014**, *136*, 2982–2985.

(20) Jiao, J.; Tan, C.; Li, Z.; Liu, Y.; Han, X.; Cui, Y. Design and Assembly of Chiral Coordination Cages for Asymmetric Sequential Reactions. *J. Am. Chem. Soc.* **2018**, *140*, 2251–2259.

(21) van Leeuwen, P. W. N. M. *Supramolecular Catalysis*; John Wiley & Sons, **2008**.

(22) Leenders, S. H. A. M.; Gramage-Doria, R.; de Bruin, B.; Reek, J. N. H. Transition metal catalysis in confined spaces. *Chem. Soc. Rev.* **2015**, *44*, 433–448.

(23) Bolliger, J. L. *Self-Assembled Coordination Cages and Organic Capsules as Catalytic Supramolecular Reaction Vessels;* Springer International Publishing, Cham, **2017**, 17–48. In *Effects of Nanoconfinement in Catalysis* (ed. Poli, R.)

(24) Furukawa, H.; Cordova, K. E.; O'Keeffe, M.; Yaghi, O. M. The chemistry and applications of metal-organic frameworks. *Science* **2013**, *341*, 974.

(25) Maurin, G.; Serre, C.; Cooper, A.; Férey, G. The new age of MOFs and of their porous-related solids. *Chem. Soc. Rev.* **2017**, *46*, 3104–3107.

(26) Yuan, S.; Feng, L; Wang, K.; Pang, J.; Bosch, M.; Lollar, C.; Sun, Y.; Qin, J.; Yang, X.; Zhang, P.; Wang, Q.; Zou, L.; Zhang, Y.; Zhang, L.; Fang, Y.; Li, J.; Zhou, H.-C. Stable Metal-Organic Frameworks: Design, Synthesis, and Applications. *Adv. Mater.* **2018**, 1704303.

(27) Majewski, M. B.; Peters, A. W.; Wasielewski, M. R.; Hupp, J. T.; Farha, O. K., Metal-Organic Frameworks as Platforms Materials for Solar Fuels Catalysis. *ACS Energy Letters* **2018,** *3*, 598–611.

(28) He, Y.; Chen, F.; Li, B.; Qian, G.; Zhou, W.; Chen, B. Porous metal-organic frameworks for fuel storage. *Coord. Chem. Rev.* **2018**, *373*, 167–198.

(29) Hosono, N.; Kitagawa, S. Modular Design of Porous Soft Materials via Self-Organization of Metal-Organic Cages. *Acc. Chem. Res.* **2018**, *51*, 2437–2446.

(30) Deng, H.; Grunder, S.; Cordova, K. E.; Valente, C.; Furukawa, H.; Hmadeh, M.; Gándara, F.; Whalley, A. C.; Liu, Z.; Asahina, S.; Kazumori, H.; O'Keeffe, M.; Terasaki, O.; Stoddart, J. F.; Yaghi, O. M. Large-pore apertures in a series of metal-organic frameworks. *Science.* **2012**, *336*, 1018–1023.

(31) Fracaroli, A. M.; Furukawa, H.; Suzuki, M.; Dodd, M.; Okajima, S.; Gándara, F.; Reimer, J. A.; Yaghi, O. M. Metal-Organic Frameworks with Precisely Designed Interior for Carbon Dioxide Capture in the Presence of Water. *J. Am. Chem. Soc.*, **2014**, *136*, 8863–8866.

(32) Bin, W.; Lv, X.-L.; Feng, D.; Xie, L.-H.; Zhang, J.; Li, M.; Xie, Y.; Li, J.-R.; Zhou, H.-C. Highly Stable Zr(IV)-Based Metal-Organic Frameworks for the Detection and Removal of Antibiotics and Organics Explosives in Water. *J. Am. Chem. Soc.,* **2016**, *138*, 6204-6216.

(33) Li, P.; Chen, Q.; Wang, T. C.; Vermeulen, N. A.; Mehdi, B. L.; Dohnalkova, A.; Browning, N. D.; Shen, D.; Anderson, R.; Gómez-Gualdrón, D. A.; Cetin, F. M.; Jagiello, J.; Asiri, A. M.; Stoddart, J. F.; Farha, O. K. Hierarchically Engineered Mesoporous Metal-Organic Frameworks Toward Cell-free Immobilized Enzyme Systems. *Chem* **2018,** *4*, 1022–1034.

(34) Jiang, H.; Jia, J.; Shkurenko, A.; Chen, Z.; Adil, K.; Belmabkhout,

Y.; Weselinski, L. J.; Assen, A. H.; Xue, D.-X.; O'Keeffe, M.; Eddaoudi, M. Enriching the Reticular Chemistry Repertoire: Merged Nets Approach for the Rational Design of Intricate Mixed-Linker Metal-Organic Framework Platforms. *J. Am. Chem. Soc.* **2018**, *140*, 8858–8867.

(35) Guillerm, V.; Grancha, T.; Imaz, I.; Juanhuix, J.; Maspoch, D. Zigzag Ligands for Transversal Design in Reticular Chemistry: Unveiling New Structural Opportunities for Metal-Organic Frameworks. *J. Am. Chem. Soc.* **2018**, *140*, 10153–10157.

(36) Ferguson, A.; Liu, L.; Tapperwijn, S. J.; Perl, D.; Coudert, F.-X.; Cleuvenbergen, S. V.; Verbiest, T.; van der Veen, M. A.; Telfer, S. G. Controlled partial interpenetration in metal-organic frameworks. *Nat. Chem.* **2016**, *8*, 250–257.

(37) Burgun, A.; Coghlan, C. J.; Huang, D. M.; Chen, W.; Horike, S.; Kitagawa, S.; Alvino, J. F.; Metha, G. F.; Sumby, C. J.; Doonan, C. J. Mapping-Out Catalytic Processes in a Metal-Organic Framework with Single-Crystal X-ray Crystallography. *Angew. Chem. Int. Ed.,* **2017**, *129*, 8532–8536.

(38) Li, P.; Vermeulen, N. A.; Malliakas, C. D.; Gómez-Gualdrón, D. A.; Howarth, A. J.; Mehdi, B. L.; Dohnalkova, A.; Browning, N. D.; O'Keeffe, M.; Farha, O. K. Bottom-up construction of a superstructure in a porous uranium-organic crystal. *Science* **2017**, *356*, 624–627.

(39) Lee, S.; Bürgi, H.-B.; Alshmimri, S. S.; Yaghi, O. M. Impact of Disordered Guest-Framework Interactions on the Crystallography of Metal-Organic Frameworks. *J. Am. Chem. Soc.* **2018**, *140*, 8958–8964.

(40) Albalad, J.; Xu, H.; Gándara, F.; Haouas, M.; Martineau-Corcos, C.; Mas-Ballesté, R.; Barnett, S. A.; Juanhuix, J.; Imaz, I.; Maspoch, D. Single-Crystal-to-Single-Crystal Postsynthetic Modification of a Metal-Organic Framework via Ozonolysis. *J. Am. Chem. Soc.* **2018**, *140*, 2028–2031.

(41) Cadiau, A.; Adil, K.; Bhatt, P. H.; Belmabkhout, Y.; Eddaoudi, M. A metal-organic framework-based splitter for separating propylene form propane. *Science* **2016**, *353*, 137–140.

(42) Schoedel, A.; Ji, Z.; Yaghi, O. M. The role of metal-organic frameworks in a carbon-neutral energy cycle. *Nature Energy*, **2016**, *1*, 16034.

(43) Cadiau, A.; Belmabkhout, Y.; Adil. K.; Bhatt, P. M.; Pillai, R. S.; Shkurenko, A.; Martineau-Corcos, C.; Maurin, G.; Eddaoudi, M. Hydrolytically stable fluorinated metal-organic frameworks for energy-efficient dehydration. *Science* **2017**, *356*, 731–735.

(44) Han, X.; Godfrey, H. G. W.; Briggs, L.; Davies, A. J.; Cheng, Y.; Daemen, L. L.; Sheveleva, A. M.; Tuna, F.; McInnes, E. J. L.; Sun, J.; Drathen, C.; George, M. W.; Ramirez-Cuesta, A. J.; Thomas, M.; Yang, S.; Schröder, M. Reversible adsorption of nitrogen dioxide within a robust porous metal-organic framework. *Nat. Mater.* **2018**, *17*, 691–696.

(45) Chen, Z.; Li, P.; Zhang, X.; Li, P.; Wasson, M. C.; Islamoglu, T.; Stoddart, J. F.; Farha, O. K. *J. Am. Chem. Soc.* **2019**, *141*, 2900–2905.

(46) Mon, M.; Lloret, F.; Ferrando-Soria, J.; Martí-Gastaldo, C.; Armentano, D.; Pardo, E. Selective and Efficient Removal of Mercury from Aqueous Media with the Highly Flexible Arms of a BioMOF. *Angew. Chemie Int. Ed.* **2016**, *55*, 11167–11172.

(47) Navarro-Sanchez, J.; Argente-Garcia, A. I.; Moliner-Martinez, Y.; Roca-Sanjuan, D.; Antypov, D.; Campins-Falco, P.; Rosseinsky, M. J.; Marti-Gastaldo, C. Peptide Metal-Organic Frameworks for Enantioselective Separation of Chiral Drugs. *J. Am. Chem. Soc.* **2017**, *139*, 4294–4297.

(48) Zhao, X.; Wang, Y.; Li, D. S.; Bu, X.; Feng, P. Metal-organic frameworks for separation. *Adv. Mater.* **2018**, *30*, 1705189.

(49) Dhakshinamoorthy, A.; Asiri, A. M.; Garcia, H. Metal-organic frameworks catalyzed C–C and C–heteroatom coupling reactions. *Chem. Soc. Rev.* **2015**, *44*, 1922–1947.

(50) Zhang, T.; Manna, K.; Lin, W. Metal-Organic Frameworks Stabilize Solution-Inaccessible Cobalt Catalysts for Highly Efficient Broad-Scope Organic Transformations. *J. Am. Chem. Soc.* **2016**, *138*, 3241–3249.

(51) Ly Thi, H.; Fu, G.; Kondinski, A.; Bueken, B.; De Vos, D.; Vogt, T. Superactivity of MOF-808 toward Pepetide Bond Hydolysis. *J. Am. Chem. Soc.* **2018**, *140*, 6325–6335.

(52) Lan, G.; Zhu, Y.-Y.; Veroneau, S. S.; Xu, Z.; Micheroni, D.; Lin, W. Electron Injection from Photoexcited Metal-Organic Framework Ligands to Ru_2 Secondary Building Units for Visible-Light-Driven Hydrogen Evolution. *J. Am. Chem. Soc.* **2018**, *140*, 5326–5329.

(53) Zhang, X.; Huang, Z.; Ferrandon, M.; Yang, D.; Robinson, L.; Li, P.; Wang, T. C.; Delferro, M.; Farha, O. K. Catalytic chemoselective functionalization of methane on a metal-organic framework. *Nature Catalysis* **2018**, *1*, 356–362.

(54) Shen, K.; Zhang, L.; Chen, X.; Liu, L.; Zhang, D.; Han, Y.; Chen, J.; Long, J.; Luque, R.; Li. Y.; Chen, B. Ordered macro-microporous metal-organic framework single crystals *Science* **2018**, *359*, 206–210.

(55) Dong, Z.; Sun, Y.; Chu, J.; Zhang, X.; Deng, H. Multivariate Metal-Organic Frameworks for Dialing-in the Binding and Programming the Release of Drug Molecules. *J. Am. Chem. Soc.* **2017**, *139*, 14209–14216.

(56) Mon, M.; Bruno, R.; Ferrando-Soria, J.; Bartella, L.; Di Donna, L.; Talia, M.; Lappano, R.; Maggiolini, M.; Armentano, D.; Pardo, E. Crystallographic snapshots of host-guest interactions in drugs@metal-organic frameworks: towards mimicking molecular recognition processes. *Mater. Horiz.* **2018**, *5*, 683–690.

(57) Yoshioka, S.; Inokuma, Y.; Duplan, V.; Dubey, R.; Fujita, M. X-ray Structure Analysis of Ozonides by the Crystalline Sponge Method. *J. Am. Chem. Soc.* **2016**, *138*, 10140–10142.

(58) Rissanen, K. Crystallography of encapsulated molecules. *Chem. Soc. Rev.* **2017**, *46*, 2638–2648.

(59) Wada, N.; Kersten, R. D.; Iwai, T.; Lee, S.; Sakurai, F.; Kikuchi, T.; Fujita, D.; Fujita, M.; Weng, J.-K. Crystalline-Sponge-Based Structural Analysis of Crude Natural Product Extracts. *Angew. Chem. Int. Ed.* **2018**, *57*, 3671–3675.

(60) Aguilera-Sigalat, J.; Bradshaw, D. Synthesis and applications of metal-organic framework-quantum dot (QD@MOF) composites. *Coord. Chem. Rev.* **2016**, *307*, 267–291.

(61) Fortea-Pérez, F. R.; Mon, M.; Ferrando-Soria, J.; Boronat, M.; Leyva-Pérez, A.; Corma, A.; Herrera, J. M.; Osadchii, D.; Gascon, J.; Armentano, D.; Pardo, E. The MOF-driven synthesis of supported palladium clusters with catalytic activity for carbene-mediated chemistry. *Nat. Mater.* **2017**, *16*, 760–766.

(62) Kitao, T.; Zhang, Y.; Kitagawa, S.; Wang, B.; Uemura, T. Hybridization of MOFs and polymers. *Chem Soc. Rev.* **2017**, *46*, 3108–3133.

(63) Mon, M.; Rivero-Crespo, M. A.; Ferrando-Soria, J.; Vidal-Moya, A.; Boronat, M.; Leyva-Pérez, A.; Corma, A.; Hernández-Garrido, J. C.; López-Haro, M.; Calvino, J.J.; Ragazzon, G.; Credi, A.; Armentano, D.; Pardo, E. Synthesis of Densely Packaged, Ultrasmall Pt^0_2 Clusters within a Thioether-Functionalized MOF: Catalytic Activity in Industrial Reactions at Low Temperature. *Angew. Chem. Int. Ed.,* **2018**, *57*, 6186-6191.

(64) Li, B.; Zhang, Y.; Ma, D.; Ma, T.; Shi, Z.; Ma, S. Metal-Cation-Directed *de Novo* Assembly of a Functionalized Guest Molecule in the Nanospace of a Metal-Organic Framework. *J. Am. Chem. Soc.* **2014**, *136*, 1202–1205.

(65) Qiu, X.; Zhong, W.; Bai, C.; Li, Y. Encapsulation of a Metal-Organic Polyhedral in the pores of a Metal-Organic Framework *J. Am. Chem. Soc.* **2016**, *138*, 1138–1141.

(66) Cohen, S. The Postsynthetic Renaissance in Porous Solids. *J. Am. Chem. Soc.* **2017**, *139*, 2855–2863.

(67) Islamoglu, T.; Goswami, S.; Li, Z.; Howarth, A. J.; Farha, O. K.; Hupp, J. T. Postsynthetic Tuning of Metal-Organic Frameworks for Targeted Applications. *Acc. Chem. Res.* **2017,** *50*, 805–813.

(68) Zhang, L.; Yuan, S.; Feng, L.; Guo, B.; Qin, J.-S.; Xu, B.; Lollar, C.; Sun, D.; Zhou, H.-C. Pore-Environmnet Engineering with Multiple Metal sites in Rare-Earth Porphyrinic Metal-Organic Frameworks. *Angew. Chem. Int. Ed.,* **2018**, *57*, 5095-5099.

(69) Zhang, X.; Frey, B. L.; Chen, Y.-S.; Zhang, J. Topology-guided Stepwise Insertion of Three Secondary Linkers on Zirconium Metal-Organic Frameworks. *J. Am. Chem. Soc.*, **2018**, *140*, 7710–7715.

(70) Martinez, C.; Muñiz, K. Defined Palladium–Phthalimidato Catalysts for Improved Oxidative Amination. *Chem. -Eur. J.* **2016**, *22*, 7367–7370.

(71) Mon, M.; Ferrando-Soria, J.; Grancha, T.; Fortea-Pérez, F. R.; Gascon, J.; Leyva-Pérez, A.; Armentano, D.; Pardo, E. Selective

gold recovery and catalysis in a highly flexible methionine-decorated metal-organic framework. *J. Am. Chem. Soc.* **2016**, *138*, 7864–7867.

(72) Fujita, M.; Sasaki, O.; Mitsuhashi, T.; Fujita, T.; Yazaki, J.; Yamaguchi, K.; Ogura, K. On the structure of transition-metal-linked molecular squares. *Chem. Commun.* **1996**, *0*, 1535–1536.

(73) Varnholt, B.; Oulevey, P.; Luber, S.; Kumara, C.; Dass, A.; Bürgi, T. Structural Information on the Au−S Interface of Thiolate-Protected Gold Clusters: A Raman Spectroscopy Study. *J. Phys. Chem. C* **2014**, *118*, 9604−9611.

(74) Gao, S.; Huang, Y.; Cao, M.; Liu, T.-f.; Cao, R. The fabrication of palladium–pyridyl complex multilayers and their application as a catalyst for the Heck reaction. *J. Mater. Chem.* **2011**, *21*, 16467–16472.

(75) Huynh, W. U.; Dittmer, J. J.; Alivisatos, A. P. Hybrid Nanorod-Polymer Solar Cells. *Science* **2002**, *295*, 2425–2427.

(76) Adamo, C.; Amatore, C.; Ciofini, I.; Jutand, A.; Lakmini, H. Mechanism of the Pd-Catalyzed Homocoupling of Arylboronic Acids: Key Involvement of a Pd Peroxo Complex. *J. Am. Chem. Soc.* **2006**, *128*, 6829–6836.

(77) Steinhoff, B. A.; Guzei, I. A.; Stahl, S. S. Mechanistic Characterization of Aerobic Alcohol Oxidation Catalyzed by $Pd(OAc)_2$/Pyridine Including Identification of the Catalyst Resting State and the Origin of Nonlinear [Catalyst] Dependence. *J. Am. Chem. Soc.* **2004**, *126*, 11268–11278.

(78) Hull, K. L.; Sanford, M. S. Mechanism of Benzoquinone-Promoted Palladium-Catalyzed Oxidative Cross-Coupling Reactions. *J. Am. Chem. Soc.* **2009**, *131*, 9651–9653.

(79) Iwasawa, T.; Tokunaga, M.; Obora, Y.; Tsuji, Y. Homogeneous Palladium Catalyst Suppressing Pd Black Formation in Air Oxidation of Alcohols *J. Am. Chem. Soc.* **2004**, *126*, 6554–6555.

(80) Leyva-Pérez, A.; Doménech-Carbó, A.; Corma, A. Unique distal size selectivity with a digold catalyst during alkyne homocoupling. *Nat. Commun.* **2015**, *6*, 6703.

(81) White, P. B.; Jaworski, J. N.; Zhu, G. H.; Stahl, S. S. Diazafluorenone-Promoted Oxidation Catalysis: Insights into the Role of Bidentate Ligands in Pd-Catalyzed Aerobic Aza-Wacker Reactions. *ACS Catal.* **2016**, *6*, 3340–3348.

(82) Toledo, A.; Funes, I.; Maseras, F.; Carmen Albeniz, A. Palladium-Catalyzed Aerobic Homocoupling of Alkynes: Full Mechanistic Characterization of a More Complex Oxidase-type Behavior. *ACS Catal.* **2018**, *8*, 7495–7506.

(83) Natte, K.; Chen, J.; Neumann, H.; Beller, M.; Wu, X. Palladium-catalyzed oxidative carbonylative coupling of arylboronic acids with terminal alkynes to alkynones. *Org. Biomol. Chem.* **2014**, *12*, 5590–5593.

(84) Devarajan, N.; Karthik, M.; Suresh, P. Copper catalyzed oxidative homocoupling of terminal alkynes to 1,3-diynes: a Cu3(BTC)2 MOF as an efficient and ligand free catalyst for Glaser–Hay coupling. *Org. Biomol. Chem.*, **2017**, *15*, 9191–9199.

(85) Zhou, Z.; Liu, M.; Wu, X.; Yu, H.; Xu, G.; Xie, Y. Amine-bridged bis(phenol) ligands for efficient Pd-catalyzed aqueous C-C coupling reactions. *Appl. Organometal. Chem.* **2013**, *27*, 562–569.

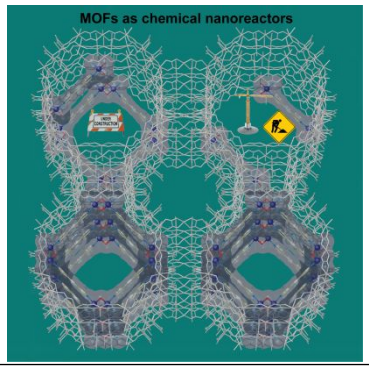
MOFs as chemical nanoreactors